Electronic Supporting information

A Multifunctional Chitosan-Anchored Copper(I)Oxide/Zinc Oxide Nanoplatform for High-Capacity Fluoride Capture in Eco-Intelligent Water Systems

Manojna R. Nayak,[a] Ravindra R. Kamble,[a,*] Vishwa B. Nadoni,[a] Mallika Wali,[a] Amruta Patri,[a] Ashok M. Sajjan[b]

[a] *Department of Studies in Chemistry, Karnatak University, Dharwad, 580003, India*
[b] *Department of Chemistry, KLE Technological University, Hubballi, 580031, India*

Table of Contents

1. Collection of *Spathodea campanulata* buds and extraction of liquid.

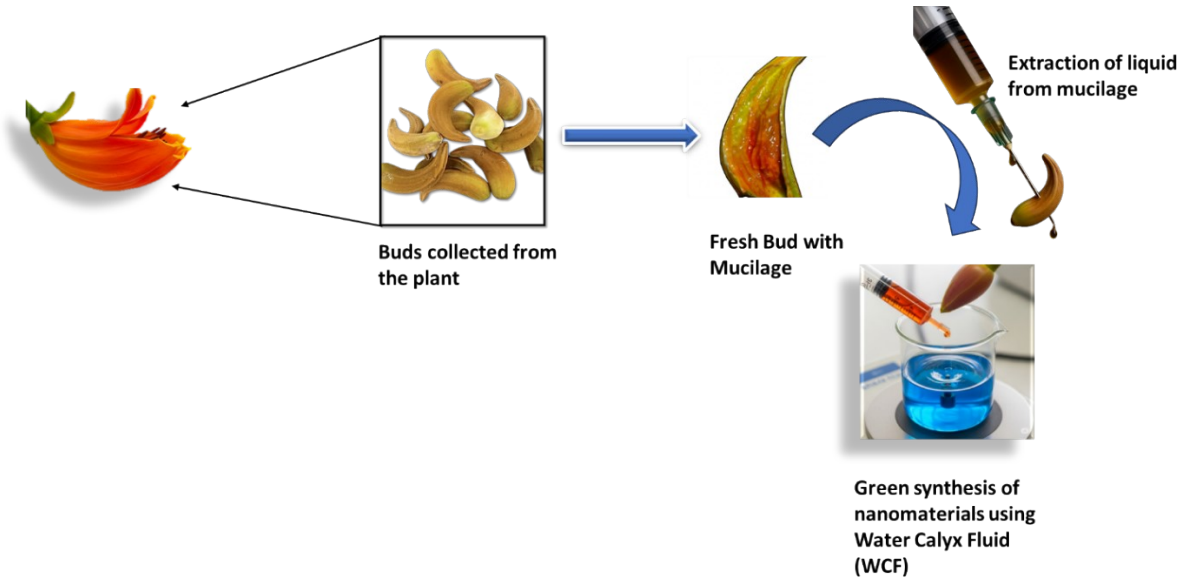

Fig. S1. Extraction process of *Spathodea campanulata* water calyx fluid (WCF).

2. UV-Vis spectrum of *Spathodea campanulata*

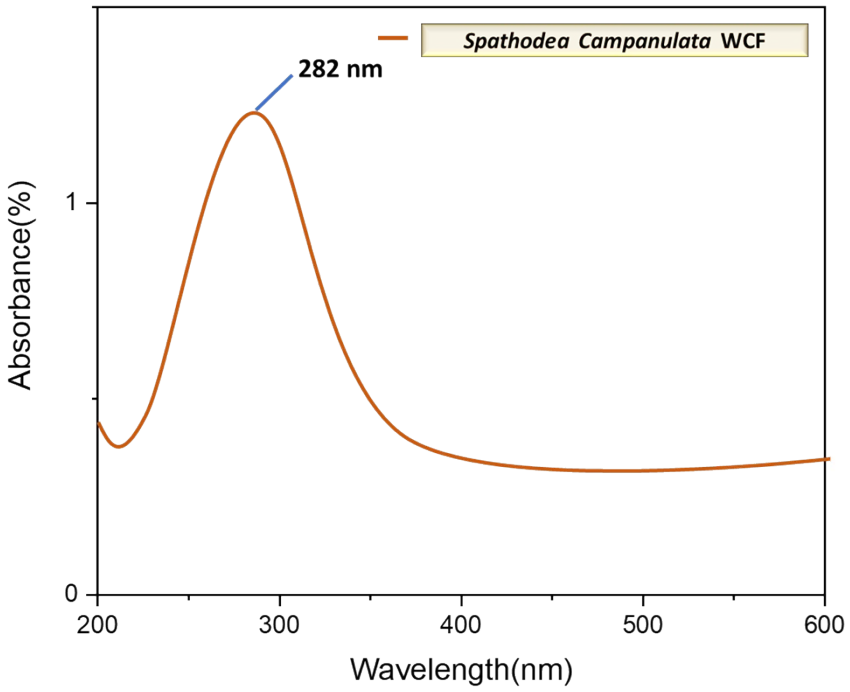

Fig. S2. UV-Visible spectrum of *Spathodea campanulata* water calyx fluid.

The UV–Visible spectral analysis of *Spathodea campanulata* water calyx fluid (WCF) offers profound insight into its intricate phytochemical milieu while concurrently delineating its operative significance in nanomaterial biogenesis. The spectrum is typified by conspicuous absorption maxima emanating from an array of polyphenolic consortia, including flavonoids, tannins, phenolics, and anthocyanins metabolites universally extolled for their redox versatility and molecular capping propensities. The salient absorption band within the 270–290 nm corridor is unequivocally ascribed to π→π* transitions inherent to extended aromatic scaffolds and conjugated carbonyl chromophores, emblematic of phenolic and flavonoid frameworks. Such delocalized π-electronic architectures confer facile electron mobilization, thereby enabling these biomolecules to function as potent reducing mediators, driving the transformation of metal precursors into nanoscale entities.

2. FTIR spectrum of *Spathodea Campanulata* water calyx fluid

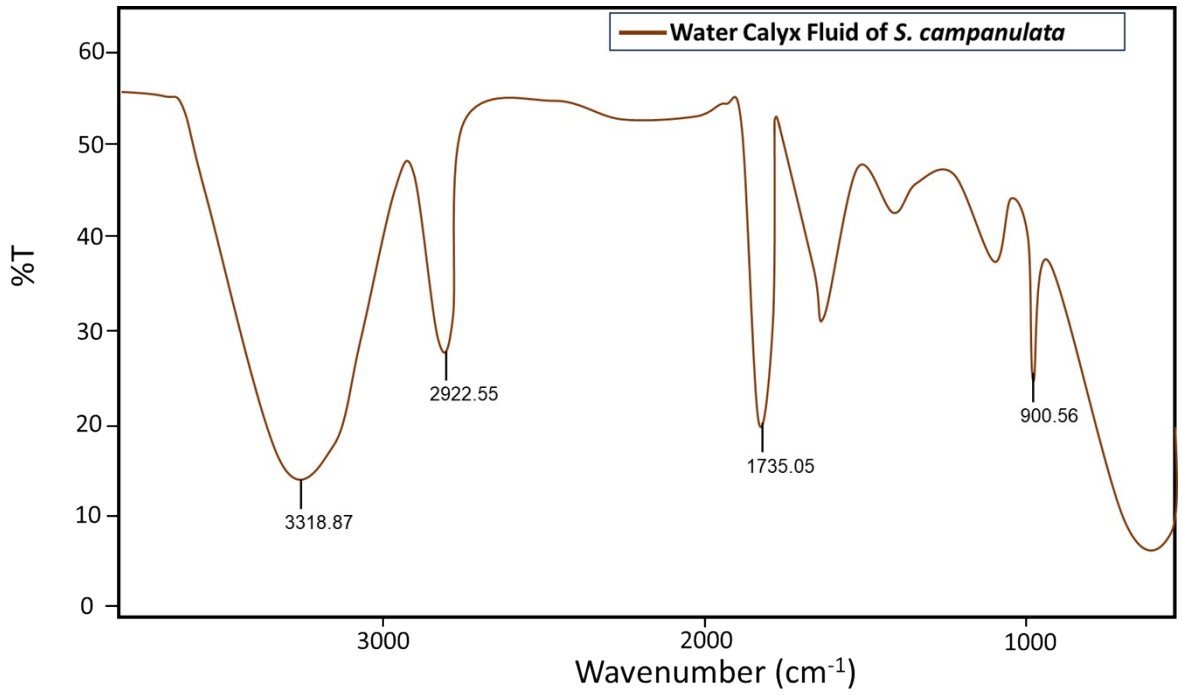

Fig. S3. FTIR spectrum of *Spathodea campanulata* Water Calyx Fluid.

The FTIR spectrum of *Spathodea campanulata* water calyx fluid (WCF) delineates a complex molecular framework that underscores the diversity of its phytochemical repertoire. The broad, intense absorption band at 3318 cm^{-1} corresponds to O–H stretching vibrations of hydroxyl functionalities, emblematic of phenolics and alcohols, and indicative of extensive hydrogen bonding among bioactive constituents. The band observed at 2922 cm^{-1} is ascribed to aliphatic C–H stretching of saturated hydrocarbons, reflecting the presence of terpenoid or fatty acid

derivatives. A distinct peak at 1735 cm^{-1} signifies carbonyl (C=O) stretching, attributable to esters, aldehydes, or other oxidized phytometabolites typically encountered in plant extracts.

The absorption near 1647 cm^{-1} is consistent with aromatic C=C stretching or conjugated C=O vibrations, reinforcing the abundance of flavonoids and other conjugated aromatic frameworks. Strong bands in the 1242–1048 cm^{-1} domain can be assigned to C–O stretching vibrations of alcohols, ethers, and glycosidic linkages, suggesting the presence of polysaccharides and secondary metabolites with oxygenated functionalities. The fingerprint region (900–650 cm^{-1}) reveals characteristic aromatic C–H bending vibrations, confirming the prevalence of aromatic phytoconstituents.

Taken together, these vibrational signatures validate the phytochemical complexity of *S. campanulata* WCF, highlighting the coexistence of hydroxyl, carbonyl, aromatic, and glycosidic groups that endow the extract with dual functionalities as a robust reducing agent for metal ion biotransformation and as a stabilizing matrix to prevent nanoparticle aggregation. This molecular richness rationalizes its efficacy as a sustainable medium for green nanomaterial synthesis.

3. Comparative Adsorption Efficiency of Different Fluoride Adsorbents.

Table S1. Evaluating the Relative Adsorption Performance of Different Fluoride Adsorbents.

Adsorbent Material	**Adsorption Capacity (mg/g)**	**Key Features / Notes**	**Reference**
Activated Alumina	1.2 – 1.8	Inexpensive, widely used, but poor efficiency at neutral pH	Roy et al., 2021
Acid-activated Alumina (AAA)	69.5	Enhanced surface activity after acid treatment	Karunanithi et al., 2019
Mg–Al Mixed Oxide (Mg/Al = 1:2)	45.3	Ion-exchange mechanism, moderate capacity	Singh et al., 2008
γ-Al_2O_3/γ-Fe_2O_3	105.0	Nanostructured mixed	Roy et al.,

Nanocomposite		oxide, moderate fluoride uptake	2021
Pectin-based Fe–Al–Ni Trimetallic Composite (PFAN)	285.0	Biopolymer-assisted composite, improved adsorption	Sharma et al., 2017
Chitosan/Fe–Al Oxide Nanocomposite	310 – 350	Biopolymer matrix with metal oxide reinforcement	Ramesh et al., 2019
Cs-Cu_2O/ZnO nanocomposite (Present Study)	~1000.0	Rich in hydroxyl, amino, carbonyl, and aromatic groups from chitosan + phytochemicals; Cu_2O/ZnO synergy enhances active sites; eco-friendly green synthesis	Present work

4. GCMS profile of *Spathodea Campanulata* Water Calyx Fluid

Table S2. Phytochemical Composition of *Spathodea campanulata* Water Calyx Fluid via GC–MS Analysis (Martin et al., 2019; Khandbahale et al., 2022).

Compound Name	**Molecular Formula**	**Major Class**	**Reported Bioactivity**
2,4-Di-tert-butylphenol	$C_{14}H_{22}O$	Phenolic compound	Antioxidant, antimicrobial
Hexadecanoic acid (Palmitic acid)	$C_{16}H_{32}O2$	Fatty acid	Antimicrobial, anti-inflammatory
Phytol	$C_{20}H_{40}O$	Diterpene alcohol	Antioxidant, anticancer, antimicrobial
Octadecanoic acid (Stearic acid)	$C_{18}H_{36}O_2$	Fatty acid	Emollient, antibacterial
Squalene	$C_{30}H_{50}$	Triterpene	Antioxidant, anticancer, immunomodulatory
Linoleic acid ethyl ester	$C_{20}H_{36}O_2$	Fatty acid ester	Hypocholesterolemic, antioxidant
β-Sitosterol	$C_{29}H_{50}O$	Phytosterol	Anti-inflammatory, cholesterol-lowering
Campesterol	$C_{28}H_{48}O$	Phytosterol	Antioxidant, cardioprotective
Stigmasterol	$C_{29}H_{48}O$	Phytosterol	Antiarthritic, anticancer,

			antimicrobial
Anthraquinone derivative	$C_{14}H_8O_2$	Polyphenolic	Antimicrobial, anticancer, antioxidant

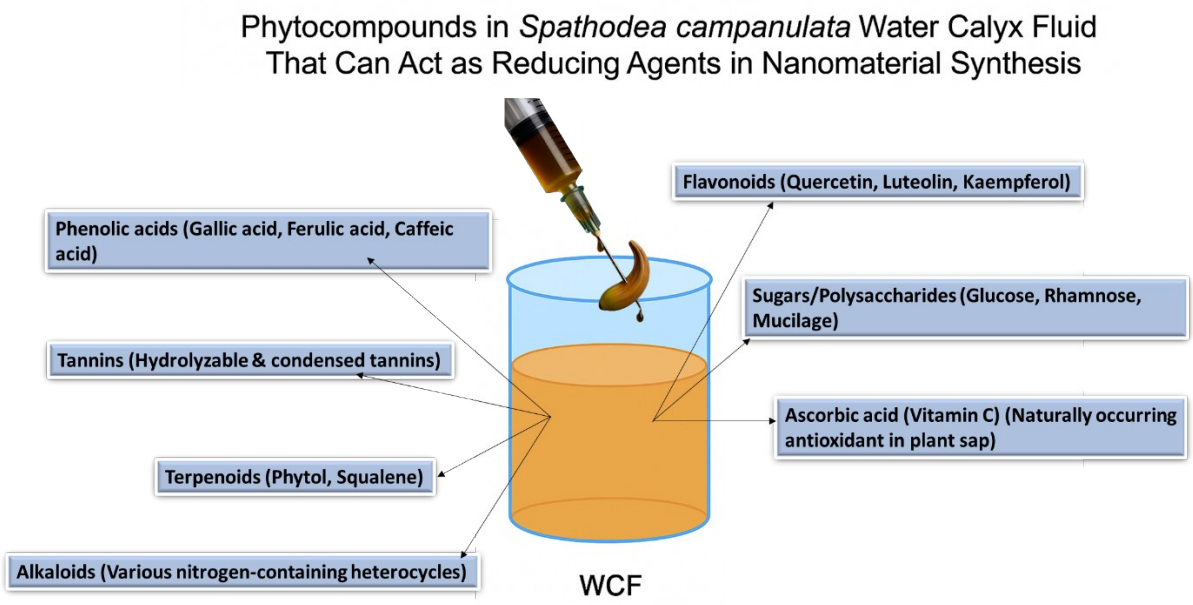

Fig. S4. Bioactive compounds present in Spathodea campanulata water calyx fluid that facilitate the reduction process during CS-Cu_2O/ZnO nanocomposite formation.

Example: The relatively high adsorption capacity (~1000 mg g^{-1}) observed for the Cs–Cu_2O/ZnO nanocomposite can be attributed to the synergistic effect of the chitosan matrix and metal oxide components. The presence of abundant surface functional groups such as $–NH_2$ and –OH in chitosan provides active binding sites for fluoride ions through electrostatic interaction and hydrogen bonding. In addition, the Cu_2O and ZnO nanoparticles contribute to enhanced surface heterogeneity and metal–fluoride interactions, which further promote adsorption. The porous structure and high surface area of the nanocomposite facilitate greater accessibility of adsorption sites, thereby resulting in improved fluoride uptake compared with many previously reported adsorbents.

For example, when the initial fluoride concentration (C_0) was 1000 mg L^{-1} and the equilibrium concentration (C_e) decreased to 0 mg L^{-1} using 0.05 g of adsorbent in 0.05 L solution, the adsorption capacity was calculated as:

$$q_e = \frac{(1000 - 0) \times 0.05}{0.05} = 1000 \text{ mg g}^{-1}$$

Table S3. Effect of Coexisting Ions on Fluoride Adsorption by CS–Cu_2O/ZnO Nanocomposite.

Coexisting Ion	Concentration (mg L^{-1})	Fluoride Removal Efficiency (%)	Observations
None (Control)	—	98.5 ± 1.2	Maximum adsorption
Cl^-	50	96.8 ± 1.5	Negligible interference
SO_4^{2-}	50	95.2 ± 1.7	Slight competition
HCO_3^-	50	93.6 ± 1.9	Moderate interference
NO_3^-	50	96.0 ± 1.4	Minimal effect
PO_4^{3-}	50	90.5 ± 2.1	Significant competition
CO_3^{2-}	50	92.8 ± 1.8	pH-related effect

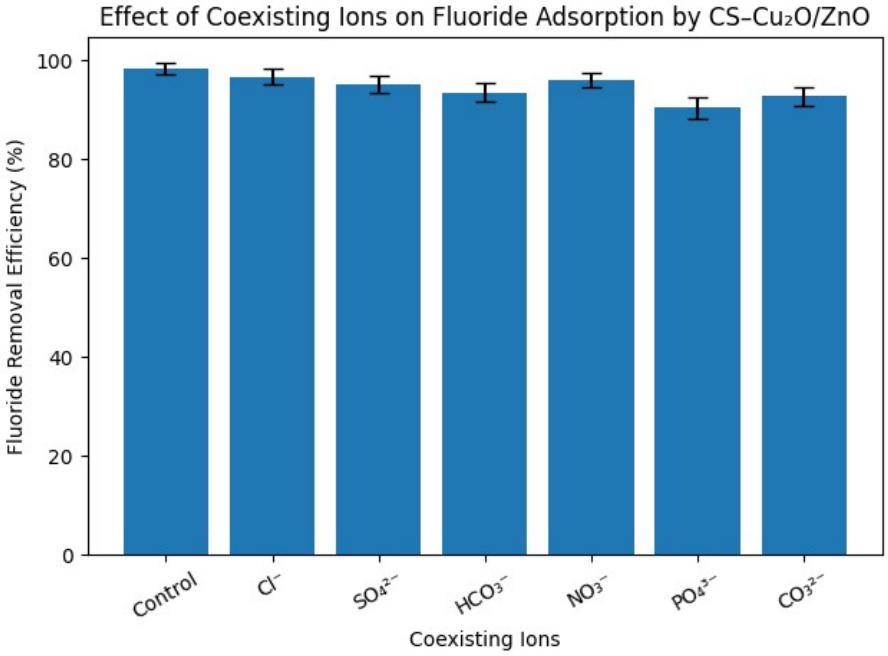

Fig. S5. Effect of coexisting ions on fluoride adsorption by CS–Cu_2O/ZnO nanocomposite. Error bars represent standard deviation (n = 3).

Table S4. Fluoride Adsorption in Model vs Real Water Matrices and Matrix-Suppression Coefficient

Water Matrix	Initial Fluoride (mg L^{-1})	Adsorption Capacity, q_e (mg g^{-1})	Removal Efficiency (%)	MSC (q_e,real / q_e,model)
Model Water	100	980.0 ± 12.5	98.5 ± 1.2	1.00
Tap Water	100	945.0 ± 15.2	95.1 ± 1.5	0.96
Groundwater Sample	100	910.0 ± 18.4	92.3 ± 1.8	0.93

Table S5. Cycling Performance and Regeneration Efficiency of the Nanocomposite.

Cycle	Removal efficiency (%)	Capacity retention (%)	Mass loss (%)	Cu leaching (mg L^{-1})	Zn leaching (mg L^{-1})
1	98.5 ± 1.2	100	—	ND	ND
2	96.2 ± 1.5	97.6	1.2	0.005	0.007
3	93.8 ± 1.7	95.2	2.0	0.007	0.009
4	91.5 ± 1.8	92.9	2.8	0.009	0.011
5	88.7 ± 2.0	90.0	3.5	0.011	0.013

ND = Not detected. Values represent mean ± standard deviation (n = 3).

References:

Karunanithi T., Palanivelu K., Meenakshi S., 2019. A novel acid modified alumina adsorbent with enhanced defluoridation property. Journal of Environmental Management, 235, 358–367.

Khandbahale D.S., 2022. Investigation of 'African Tulip Tree-Calyx Water' as a novel nutritional supplement and novel food source. Science, Technology and Development, 11(2), 447–449.

Martin P.A., Jayanthi D., Thamizhseran N., 2019. Bio-Physicochemical studies on water calyx fluid in the African Tulip Tree, Spathodea campanulata P. Beauv. Pharmacognosy Journal, 11(3), 594–599.

Ramesh S., Radhakrishnan S., Kannan N., 2019. Chitosan-based nanocomposite incorporated with Fe–Al oxide for defluoridation of drinking water. Journal of Hazardous Materials, 367, 629–639.

Roy S., Chattoraj S., Mukherjee A., 2021. Recently developed adsorbing materials for fluoride removal from contaminated drinking water: A review. Sustainability, 13, 7061.

Sharma G., Naushad M., Kumar A., Al-Muhtaseb A.H., Ghfar A.A., Khan M.R., Stadler F.J., 2017. Comparative kinetics and thermodynamic studies of removal of Cr(VI) and Pb(II)

using a new composite: Pectin-based Fe–Al–Ni trimetallic oxide nanocomposite. Chemical Engineering Journal, 308, 438–447.

Singh T.S., Pant K.K., 2008. Mg–Al mixed oxide adsorbent for defluoridation of drinking water. Journal of Hazardous Materials, 155, 423–430.